

## Anomalous Hall Effect and Topological Defects in Antiferromagnetic Weyl Semimetals: $\text{Mn}_3\text{Sn}/\text{Ge}$

Jianpeng Liu and Leon Balents

*Kavli Institute for Theoretical Physics, University of California, Santa Barbara, California 93106, USA*  
(Received 12 May 2017; published 24 August 2017)

We theoretically study the interplay between bulk Weyl electrons and magnetic topological defects, including magnetic domains, domain walls, and  $\mathbb{Z}_6$  vortex lines, in the antiferromagnetic Weyl semimetals  $\text{Mn}_3\text{Sn}$  and  $\text{Mn}_3\text{Ge}$  with negative vector chirality. We argue that these materials possess a hierarchy of energy scales, which allows a description of the spin structure and spin dynamics using an  $XY$  model with  $\mathbb{Z}_6$  anisotropy. We propose a dynamical equation of motion for the  $XY$  order parameter, which implies the presence of  $\mathbb{Z}_6$  vortex lines, the double-domain pattern in the presence of magnetic fields, and the ability to control domains with current. We also introduce a minimal electronic model that allows efficient calculation of the electronic structure in the antiferromagnetic configuration, unveiling Fermi arcs at domain walls, and sharp quasibound states at  $\mathbb{Z}_6$  vortices. Moreover, we have shown how these materials may allow electronic-based imaging of antiferromagnetic microstructure, and propose a possible device based on the domain-dependent anomalous Hall effect.

DOI: 10.1103/PhysRevLett.119.087202

The anomalous Hall effect (AHE) [1,2] has been a nucleation center for geometry and topology in the physics of solids. The concepts of Berry curvatures and topology unveil broad applications to electronic systems in the form of topological insulators, superconductors [3,4], and semimetals with topological Weyl (and other) fermion excitations [5–18]. The AHE reappears as one of the key emergent properties of topological semimetals.

The dissipationless nature of the AHE also makes it interesting for applications. Antiferromagnetic realizations of AHE may be of practical interest for the sake of miniaturization, but the microscopic magnetic structure, the spin dynamics, and the AHE of antiferromagnets are relatively uninvestigated. Here we attack these issues in the family of noncollinear antiferromagnets including  $\text{Mn}_3\text{Sn}$  and  $\text{Mn}_3\text{Ge}$ , for which a strong AHE was predicted and then experimentally verified to exist [19–22]. First principles calculations further indicate that in  $\text{Mn}_3\text{Sn}$  and  $\text{Mn}_3\text{Ge}$  there are Weyl nodes around the Fermi level [23,24]. We argue that these materials possess a hierarchy of energy scales that permits a description of the microstructure and spin dynamics as an  $XY$  model with  $\mathbb{Z}_6$  anisotropy. We propose a dynamical equation of motion for the  $XY$  order parameter, which implies a rich domain structure, the presence of  $\mathbb{Z}_6$  vortex lines, and the ability to control domains with current. We further introduce a minimal electronic model that allows efficient calculation of the electronic structure in a textured antiferromagnetic configuration, unveiling Fermi arcs at domain walls, and quasibound states at  $\mathbb{Z}_6$  vortices. We show how these materials may allow electronic-based imaging of antiferromagnetic microstructure and propose a possible device based on domain-dependent AHE.

*Symmetry and the microscopic spin model.*—The  $\text{Mn}_3\text{Sn}$ -class material crystallizes in hexagonal lattice structure with space group  $P6_3/mmc$  as shown in Figs. 1(a) and 1(b). Taking  $\text{Mn}_3\text{Sn}$  as an example, each  $\text{Mn}^{4+}$  ion has a large classical spin  $\sim 2-3 \mu_B$  [25,26] forming a layered kagomé lattice. The system orders antiferromagnetically in a  $120^\circ$  noncollinear structure as shown in Fig. 1(c), with the Neel temperature  $T_N \approx 420$  K [25–28]. This may be understood from the hierarchy of interactions typical for  $3d$  transition metal ions: Heisenberg exchange is largest, followed by

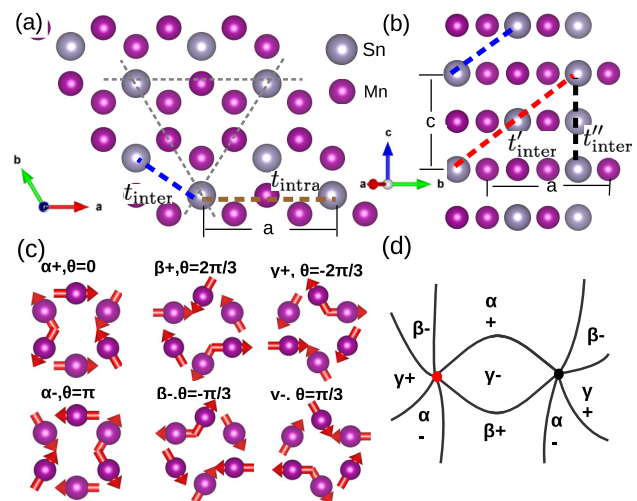


FIG. 1. (a) The lattice structure of  $\text{Mn}_3\text{Sn}$  from a top view, and (b) a side view. The thick dashed lines with brown, red, and blue colors indicate different hopping processes of the tight-binding model introduced in the text. The gray dashed lines in (a) indicate the easy axes. (c) The six magnetic domains. (d) Schematic illustration of the  $\mathbb{Z}_6$  vortex lines.

Dzyaloshinskii-Moriya (DM) interaction, with single-ion anisotropy (SIA) being the weakest effect. The former two terms select an approximately  $120^\circ$  pattern of spins with negative vector chirality, which leaves a  $U(1)$  degeneracy: any rotation of spins within the  $ab$  plane leaves the energy unchanged, when the SIA is neglected. Therefore, the system can be described by the following microscopic spin Hamiltonian:

$$H_s = J_1 \sum_{\langle ij \rangle_{xy}} \mathbf{S}_i \cdot \mathbf{S}_j + J_2 \sum_{\langle ij \rangle_z} \mathbf{S}_i \cdot \mathbf{S}_j + \sum_{\langle ij \rangle_{xy}} \mathbf{D}_{ij} \cdot \mathbf{S}_i \times \mathbf{S}_j - \sum_i K(\hat{\mathbf{n}}_i \cdot \mathbf{S}_i)^2. \quad (1)$$

Here the spin  $\mathbf{S}_i$  is a classical vector with fixed length  $m_s$ . The positive constants  $J_1$ ,  $J_2$  are isotropic exchange interactions between intraplane and interplane nearest-neighbor spins, which include contributions mediated by itinerant electrons, i.e., Ruderman-Kittel-Kasuya-Yosida (RKKY) couplings. We include an in-plane Dzyaloshinskii-Moriya interaction specified by the vector  $\mathbf{D}_{ij} = D\hat{\mathbf{z}} + D'\hat{\mathbf{z}} \times \hat{\mathbf{e}}_{ij}$ , where  $\hat{\mathbf{e}}_{ij}$  is the unit vector oriented from site  $i$  to site  $j$ .  $\hat{\mathbf{n}}_i$  is the unit vector characterizing the local easy axis at site  $i$ . From Eq. (1) we can determine nearly all the properties of the classical kagomé antiferromagnet. In particular, we find that the  $\mathbb{Z}_6$  anisotropy  $\lambda$  is  $\mathcal{O}(K^3)$ ,  $\lambda = K^3 m_s^2 / 12(J_1 + J_2)^2$ . The SIA  $K$  and the in-plane DM interaction  $D'$  lead to both in-plane and out-of-plane cantings of the magnetic moment,

$$\begin{aligned} \mathbf{M}_{\perp c} &= \frac{K g m_s}{J_1 + J_2} (\cos \theta, \sin \theta, 0), \\ M_z &= -\frac{D' K g m_s}{\sqrt{3}(J_1 + J_2)^2} \sin 3\theta, \end{aligned} \quad (2)$$

where  $g$  denotes the Landé  $g$  factor. The  $z$ -component magnetization  $|M_z|$  vanishes when  $\theta$  is  $2\pi n/6$  ( $\lambda > 0$ ), i.e., when the local easy axis points from the Mn to the nearest-neighbor Sn, which we believe is the ground state for  $\text{Mn}_3\text{Sn}$ . On the other hand,  $|M_z|$  is maximized when  $\theta = (2n+1)\pi/6$  ( $\lambda < 0$ ), which may lead to small in-plane anomalous Hall conductivity, as is the case in  $\text{Mn}_3\text{Ge}$  [21,22].

The in-plane and out-of-plane magnetic susceptibilities are also derived from Eq. (1), from which we can evaluate the microscopic interaction parameters by comparing the susceptibility formula to the corresponding experimental data [21]. We find that  $J_1 + J_2 = 5.606$  meV,  $D = 0.635$  meV, and  $K = 0.187$  meV (see Supplemental Material [29]).

*Order parameter, free energy, and implications.*—From Eq. (1) we derive a phenomenological free energy for the system with an  $XY$  order parameter  $\psi = m_s e^{-i\theta}$ , where  $m_s$  is the magnitude of the local spin moment, and  $\theta$  is (minus) the angle of some specific spin in the plane. We focus on the ordered phase, in which  $m_s$  is uniform, and the free energy may be written in terms of  $\theta$  alone. Symmetry dictates the form

$$F_s = \int d^3\mathbf{r} \left( \frac{\rho}{2} |\nabla\theta(\mathbf{r})|^2 + \rho_1 |\hat{\mathbf{K}}(\theta) \cdot \nabla\theta|^2 - \lambda \cos 6\theta(\mathbf{r}) - \gamma \mathbf{B} \cdot \hat{\mathbf{K}} \right). \quad (3)$$

Here  $\rho$  and  $\rho_1$  are isotropic and anisotropic stiffnesses;  $\lambda$  is a  $\mathbb{Z}_6$  anisotropy. We also introduced the  $XY$  unit vector  $\hat{\mathbf{K}} = (\cos \theta, \sin \theta, 0)$ , which describes coupling  $\gamma$  to a uniform magnetic field  $\mathbf{B}$  (which occurs due to small in-plane canting of the moments [25,26,28]). Equation (3) is derived from the microscopic spin Hamiltonian Eq. (1), which allows us to estimate these parameters. We estimate  $\rho \approx 0.568$  meV/Å,  $\rho_1 \approx 0.011$  meV/Å, and  $\lambda \approx 1.159 \times 10^{-7}$  meV/Å<sup>3</sup> at temperature 50 K (see Supplemental Material [29]).

The  $\mathbb{Z}_6$  structure of the free energy implies the existence of six minimum energy domains in which  $\theta$  maximizes  $\lambda \cos 6\theta$ . We take  $\lambda > 0$ , for which this is  $\theta = 2\pi n/6$ , with  $n = 0, \dots, 5$ . It is convenient to label them as  $\alpha^{+-}$ ,  $\beta^{+-}$ , and  $\gamma^{+-}$  as shown in Fig. 1(c), with the  $\pm$  superscript denoting domains that are time-reversal conjugates.

The long-time dynamics follows from the free energy and the Langevin equation (see chapter 9 of Ref. [30])

$$\frac{\partial\theta(\mathbf{r}, t)}{\partial t} = -\mu \frac{\delta F_s}{\delta\theta(\mathbf{r}, t)} + \mu\eta(\mathbf{r}, t) + f(\mathbf{j}), \quad (4)$$

where  $\eta(\mathbf{r}, t)$  represents a random thermal fluctuation at temperature  $T$  obeying the Gaussian distribution of zero mean.  $\mu$  is the damping factor, and hereafter is set to 1. The final term  $f(\mathbf{j})$  represents nonequilibrium forces to be discussed later. Neglecting  $\rho_1$  and for  $\mathbf{B} = 0$ , Eq. (4) becomes the famous (overdamped) sine-Gordon equation. Its stationary solutions include a domain wall with a width  $\pi\sqrt{\rho/\lambda}/6 \sim 110$  nm using our estimates. Significantly, the elementary domain walls connect states that differ by  $\Delta\theta = \pi/3$ , which are not time-reversal conjugates. The  $\rho_1$  term leads to orientation dependence of the domain wall energy, and, e.g., faceting of domain boundaries. Six of these minimal domain walls meet at curves in three dimensions, which define  $\mathbb{Z}_6$  vortex lines [see Fig. 1(d)], around which  $\theta$  winds by  $\pm 2\pi$ .

To observe the microstructure, we carried out a numerical simulation of a thin slab, assuming homogeneity in the  $z$  direction and discretizing the two-dimensional continuum model with an effective lattice constant of  $a_{cg} = 600$  Å (see Supplemental Material [29]). Figure 2(a) shows the equilibrium spin configuration resulting from a quench from a random initial state of a  $576 \mu\text{m}^2$  sample in zero applied field. Clearly there are six types of domains in the figure, marked by  $\alpha^\pm$ ,  $\beta^\pm$ , and  $\gamma^\pm$ . These sixfold domains merge at the vortices and antivortices marked by white and black dots, respectively.

In Fig. 2(b), we show the spin configuration resulting from the same preparation but with an applied magnetic

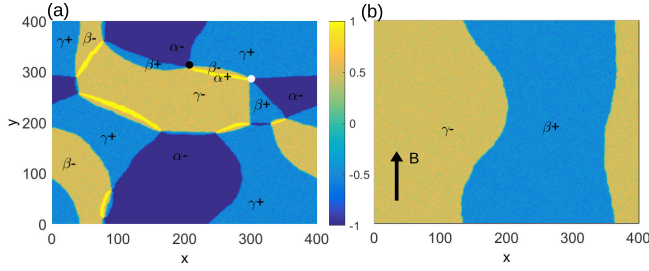


FIG. 2. The spin configurations on the coarse-grained lattice at time  $t = 9600$  obtained from numerical simulations of the Langevin equation: (a) without any magnetic field, and (b) an external magnetic field  $B = 0.005$  T is applied along the  $y$  direction.

field of  $B = 0.005$  T along the  $[120]$  axis ( $y$  axis). As is clearly shown in the figure, the field preferentially selects just two degenerate  $\beta^+$  ( $\cos\theta = -1/2$ ) and  $\gamma^-$  ( $\cos\theta = 1/2$ ) domains. The orientation of the domain wall, which tends to be normal to the  $[100]$  direction, is fixed by the anisotropic stiffness term.

*Minimal electronic model and electronic structure.*—In order to study the electronic properties in the presence of magnetic textures with large-scale spatial variations, we introduce a minimal four-band tight-binding (TB) model with a single spinor  $p_z$  orbital at each Sn. As indicated by the thick dashed lines in Figs. 1(a) and 1(b), we consider the following four hopping processes:

$$\begin{aligned} t_{\text{intra}}(\mathbf{r}_{nm}) &= t_0 \mathbb{1}_{2 \times 2} + t_J \boldsymbol{\sigma} \cdot \mathbf{S}_{nm} + (-1)^{\xi_{mn}} i \lambda_z \sigma_z, \\ t_{\text{inter}}(\mathbf{r}_{nm}) &= t_1 \mathbb{1}_{2 \times 2}, \\ t'_{\text{inter}}(\mathbf{r}_{nm}) &= i \lambda_R \mathbf{e}_{\text{soc}}^{\mathbf{r}_{nm}} \cdot \boldsymbol{\sigma}, \\ t''_{\text{inter}}(\mathbf{r}_{nm}) &= t_2 \mathbb{1}_{2 \times 2}, \end{aligned} \quad (5)$$

where the hopping from orbital  $m$  centered at  $\mathbf{r}_m$  to orbital  $n$  centered at  $\mathbf{r}_n$  is expressed as a  $2 \times 2$  matrix due to the spin degrees of freedom of each orbital, and  $\mathbf{r}_{nm} = \mathbf{r}_n - \mathbf{r}_m$ . The model includes three spin-independent hopping terms ( $t_0$  in-layer and  $t_1$  and  $t_2$  interlayer), a spin-dependent hopping  $t_J$  reflecting exchange coupling to the Mn moment  $\mathbf{S}$  in the middle of the bond across which the electrons hop, and two spin-orbit coupling (SOC) terms  $\lambda_z$  and  $\lambda_R$ , which are important due to the heavy nature of the Sn ions. Details on the  $\xi_{mn}$  and  $\mathbf{e}_{\text{soc}}^{\mathbf{r}_{nm}}$  parameters that define the SOC are given in Supplemental Material [29]. Hereafter we fix the parameters of the model as  $t_0 = 1$ ,  $t_1 = 0.5$ ,  $t_J = -0.5$ ,  $\lambda_z = 0.5$ ,  $t_2 = -1$ , and  $\lambda_R = 0.2$ . We arrange  $\mathbf{S}_{nm}$  spins to reflect the spin order under consideration. In the ordered state we take the spin canting angle  $\sim 1.7^\circ$ , corresponding to a net moment  $\sim 5\%$  of each Mn spin for each kagomé cell. We refer the readers to Supplemental Material [29] for more details.

The bulk band structure of the TB model introduced above in the  $\alpha^+$  domain is shown in Fig. 3(a). We find that in the  $\alpha^+$  domain [see Fig. 1(c)], there are four Weyl nodes

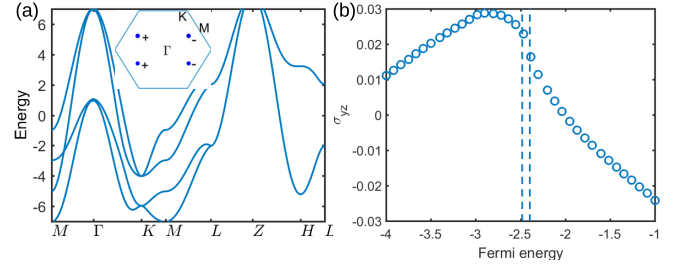


FIG. 3. (a) The bulk band structure of the tight-binding model in the  $\alpha^+$  domain with  $1.7^\circ$  spin canting. The inset indicates the positions of two different types of bulk Weyl nodes  $W_1$  and  $W_2$  in the  $k_z = 0$  plane. (b) The anomalous Hall conductivity  $\sigma_{yz}$  in the  $\alpha^+$  domain.

at  $(\pm 0.3522, 0, 0)$  and  $(\mp 0.3522, \pm 0.3522, 0)$  at energy  $E_{W1} = -2.395t_0$ , which are denoted by solid blue dots in the inset of Fig. 3(a), with the sign corresponding to the chiralities of the Weyl nodes. There are two additional band touching points with quadratic dispersions along the  $k_z$  direction at  $(0, \pm 0.3564, 0)$  at energy  $E_{W2} = -2.480t_0$ . Since the dispersion is quadratic along  $k_z$ , these two additional nodes carry zero Berry flux, and do not make significant contributions to the transport properties. The positions of the Weyl nodes in the other five domains can be obtained by applying  $C_{3z}$  and/or time-reversal operations to those of the  $\alpha^+$  domain.

*From magnetic structure to electronic properties.*—The most interesting feature of  $\text{Mn}_3\text{Sn}$  and its relatives is the strong influence of the magnetism on the electronic properties such as conductivities. In the  $\text{Mn}_3\text{Sn}$  family, crystalline symmetries and the Onsager relation tightly constrain the conductivity tensor (see Supplemental Material [29]). In general the antisymmetric part of the Hall conductivity is expressed in terms of a ‘‘Hall vector’’  $\mathbf{Q}$ , with  $\frac{1}{2}(\sigma_{\mu\nu} - \sigma_{\nu\mu}) = (e^2/2\pi h)\epsilon_{\mu\nu\lambda}Q_\lambda$ . Up to the third order in  $\psi$ , we find

$$\mathbf{Q} = q|\psi|\hat{\mathbf{K}} + \tilde{q}|\psi|^3 \text{Im}[(\hat{K}_x + i\hat{K}_y)^3]\hat{\mathbf{z}}, \quad (6)$$

where  $q|\psi|$  and  $\tilde{q}|\psi|^3$  are parameters arising from microscopic modeling. Since we expect the  $O(|\psi|^3)$  terms to be small, we observe that the Hall vector is directed along  $\hat{\mathbf{K}}$ , which lies in the  $xy$  plane. To verify these symmetry considerations, we carried out a direct calculation of the full bulk conductivity tensor of the microscopic model using the Kubo formula (see Supplemental Material [29]). We show the calculated anomalous Hall conductivity  $\sigma_{zx}$  in the  $\alpha^+$  domain in Fig. 3(b). The result is generically nonzero, but highly dependent upon the Fermi energy (the horizontal axis).

*Electronic properties associated with topological defects.*—The direct connection of the conductivity to the order parameter suggests that transport can be a fruitful probe of magnetic microstructures. When the electronic mean free path is shorter than the length scales of magnetic

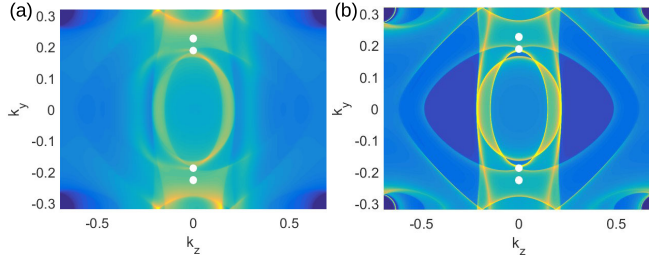


FIG. 4. (a) The surface Fermi arcs of the  $\beta^+$  domain with the surface normal vector  $\hat{x}$ . (b) The domain wall Fermi arcs with the domain wall in the  $yz$  plane. The white dots indicate the projection of Weyl nodes into the folded surface Brillouin zone.

textures, a local conductivity approximation is adequate:  $\mathbf{J}(\mathbf{r}) = \underline{\sigma}[\hat{\mathbf{K}}(\mathbf{r})]\mathbf{E}(\mathbf{r})$ . From this relation and Eq. (6), the electrostatic potential  $\Psi(\mathbf{r})$  can be determined for an arbitrary texture  $\hat{\mathbf{K}}(\mathbf{r})$ . For example, in the  $yz$  plane, the electrostatic potential  $\Psi(z, y)$  may be expanded as  $\Psi(z, y) \approx -zE_0 + E_0\phi(z, y)$ , and  $\phi(z, y)$  is determined by

$$\partial_z^2 \phi(z, y) + \frac{\sigma_{yy}}{\sigma_{zz}} \partial_y^2 \phi(z, y) = \partial_y \theta_H(z, y), \quad (7)$$

where  $E_0$  is the constant electric field,  $\theta_H(z, y) = \sigma_{yz}(z, y)/\sigma_{zz}$ , and  $\sigma_{yz}$  is proportional to  $\hat{K}_x$  as shown in Eq. (6). Through inversion, it should be possible to image the magnetic domain structure purely through a spatially resolved electrostatic measurement.

In the full quantum treatment, the electronic structure is nontrivially modified by magnetic textures. The new feature here is the appearance of Fermi arcs at domain walls. This is because a domain wall acts as a sort of internal surface, at which Fermi arc states carry chiral currents, similar to ordinary surfaces. Without loss of generality consider a minimal energy domain wall between the  $\beta^+$  and  $\gamma^-$  domains, which have  $\mathbf{K}$  at  $\pm 30^\circ$  from the  $y$  axis. The domains have Weyl points in the  $k_z = 0$  plane, with chiralities that differ in the two domains. Distinct electronic properties thus occur when this domain wall is in an  $xy$ ,  $xz$ , or  $yz$  plane of the crystal.

Figure 4(a) shows the surface spectral functions of the  $\beta^+$  domain for a [100] surface. There are three Fermi arcs connecting the two projected Weyl nodes, which are closer to the origin. Figure 4(b) shows the spectral function at the interface of the  $\beta^+$  and  $\gamma^-$  domains with the same orientation. It shows double the Fermi arcs found at the interface, i.e., six instead of three (see Supplemental Material [29] for more details).

We make two proposals to detect the presence of the domain-wall Fermi arcs. First, the in-plane transport within a domain wall may exhibit its own anomalous Hall effect. We checked that this indeed occurs for a  $\beta^+ - \gamma^-$  wall with  $zx$  orientation, by calculating  $\sigma_{zx}$  for a supercell with two domain walls spread over 30 primitive cells. We find  $\sigma_{zx} = 0.044$  for the supercell, about two times larger than the bulk

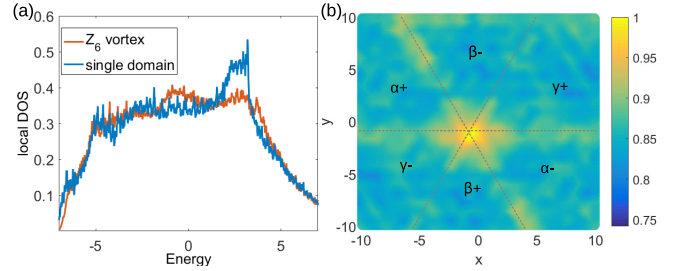


FIG. 5. (a) The energy dependence of the local DOS at the vortex line. (b) The local DOS at energy  $E = -1.15t_0$  distributed in real space with a vortex line located at the origin.

value of 0.023 found for the same cell with a single  $\beta^+$  or  $\gamma^-$  domain. This enhancement is expected whenever  $\hat{\mathbf{K}}$  is normal to the wall in its interior. Second, domain wall bound states can manifest as an intrinsic resistance across the wall, since they take away from the weight of continuum states that are strongly transmitted and hence contribute to conductance. We verified such a decreased conductance normal to the wall for all domain wall orientations in numerical studies (see Supplemental Material [29]).

While we focus on the domain walls, it is worth noting that the  $\mathbb{Z}_6$  vortex lines may have their own electronic states. Using the tight-binding model introduced above, we have numerically constructed a  $40 \times 40 \times 1$  supercell including six domains, which are merged at a vortex line. The energy dependence of the local density of states (DOS) at the vortex line is shown in Fig. 5(a), where the red (blue) line indicates the DOS in the presence (absence) of the vortex line. There are two distinct peaks of DOS that seem to be contributed by the vortex line: one at energy  $E \sim 4$ , and the other extending from  $-1.3$  to  $0.2$ . Figure 5(b) further shows the local DOS distribution in the supercell at  $E = -1.15$  in the presence of a vortex line, which indicates a sharp peak localized at the vortex line. Such quasibound states at the vortex line may be a consequence of the chiral magnetic field emerging from the winding of the  $XY$  spins around the  $\mathbb{Z}_6$  vortex line [31].

*Current-driven domain wall dynamics.*—Let us now consider the feedback of the conduction electrons on the spin texture. Given that the primary order parameter of the antiferromagnet is not the magnetization, it is unclear how consideration of the spin-transfer torque [32] applies here. Instead, we take a symmetry-based approach and ask how the current  $\mathbf{j}$  may appear as a force in the equation of motion for the easy spin angle  $\theta$ , Eq. (4). The result (see Supplemental Material [29]) is that the force takes the form

$$f(\mathbf{j}) = -\sum_a (p_a j_a \partial_a \theta + q_1 \mathbf{j} \cdot \partial_z \hat{\mathbf{K}} + q_2 j_z \nabla \cdot \hat{\mathbf{K}}). \quad (8)$$

Here  $p_x = p_y$ ,  $p_z$ ,  $q_1$ , and  $q_2$  are constants. Various arguments (see Supplemental Material [29]) suggest that  $q_1$  and  $q_2$ , which tend to drive the domain wall along the

direction perpendicular to the current flow, are much smaller than  $p_a$ , so we henceforth neglect them.

Despite the intrinsic antiferromagnetic nature of the system, the  $p_\mu$  terms appear formally very similar to spin-transfer torques. They could be understood in a hydrodynamic fashion as describing “convection” of the spin texture with or against the current flow: indeed added to Eq. (4), these terms are equivalent to a Galilean boost and consequently velocity  $v_a = \mu p_a j_a$ . This leads to concrete experimental proposals. Specifically, in the geometry of Fig. 2(b), a current applied along the  $x$  direction controls the position of the wall. The nondissipative Hall voltage measured between two contacts across the  $y$  direction at fixed  $x$  can thereby be switched by purely electrical means, as the domain wall moves to the left or right of the contacts [33].

Although the quantitative results discussed in this Letter are for  $\text{Mn}_3\text{Sn}$ , most of the key physics, such as the domain-dependent AHE, the domain wall Fermi arcs, the general form of the spin models, and the expression of the spin-transfer torque, also apply to  $\text{Mn}_3\text{Ge}$ . This is because they are derived based on symmetry considerations and topological arguments that are expected to be robust regardless of the materials’ details.

The results of this paper provide the framework to design and model the spin dynamics and topologically influenced electrical transport in the negative vector chirality antiferromagnets  $\text{Mn}_3\text{Sn}$  and  $\text{Mn}_3\text{Ge}$ , and the methodology may be applied more broadly to XY-like antiferromagnetic systems. Weyl nodes in the electronic structure induce Fermi arc bound states that influence transport in the presence of domain walls. In addition to advancing the fundamental physics of Weyl fermions in noncollinear antiferromagnets, these results mark the  $\text{Mn}_3\text{Sn}$  class of materials as promising candidates for novel magnetic storage devices.

We thank the groups of professors Satoru Nakatsuji and Yoshichika Otani for introducing us to these materials and sharing their data. This research was supported by the National Science Foundation under Grant No. DMR1506119.

---

[1] R. Karplus and J. M. Luttinger, *Phys. Rev.* **95**, 1154 (1954).  
 [2] N. Nagaosa, J. Sinova, S. Onoda, A. MacDonald, and N. Ong, *Rev. Mod. Phys.* **82**, 1539 (2010).  
 [3] M. Z. Hasan and C. L. Kane, *Rev. Mod. Phys.* **82**, 3045 (2010).  
 [4] X.-L. Qi and S.-C. Zhang, *Rev. Mod. Phys.* **83**, 1057 (2011).  
 [5] X. Wan, A. M. Turner, A. Vishwanath, and S. Y. Savrasov, *Phys. Rev. B* **83**, 205101 (2011).  
 [6] A. A. Burkov, M. D. Hook, and L. Balents, *Phys. Rev. B* **84**, 235126 (2011).  
 [7] A. A. Burkov and L. Balents, *Phys. Rev. Lett.* **107**, 127205 (2011).

[8] G. Xu, H. Weng, Z. Wang, X. Dai, and Z. Fang, *Phys. Rev. Lett.* **107**, 186806 (2011).  
 [9] S. Murakami, *New J. Phys.* **9**, 356 (2007).  
 [10] Z. Wang, Y. Sun, X.-Q. Chen, C. Franchini, G. Xu, H. Weng, X. Dai, and Z. Fang, *Phys. Rev. B* **85**, 195320 (2012).  
 [11] Z. Wang, H. Weng, Q. Wu, X. Dai, and Z. Fang, *Phys. Rev. B* **88**, 125427 (2013).  
 [12] A. M. Turner and A. Vishwanath, in *Topological Insulators* (Elsevier, 2013), p. 293.  
 [13] J. Liu and D. Vanderbilt, *Phys. Rev. B* **90**, 155316 (2014).  
 [14] H. Weng, C. Fang, Z. Fang, B. A. Bernevig, and X. Dai, *Phys. Rev. X* **5**, 011029 (2015).  
 [15] A. A. Soluyanov, D. Gresch, Z. Wang, Q. Wu, M. Troyer, X. Dai, and B. A. Bernevig, *Nature (London)* **527**, 495 (2015).  
 [16] S.-Y. Xu, I. Belopolski, N. Alidoust, M. Neupane, G. Bian, C. Zhang, R. Sankar, G. Chang, Z. Yuan, C.-C. Lee *et al.*, *Science* **349**, 613 (2015).  
 [17] L. Yang, Z. Liu, Y. Sun, H. Peng, H. Yang, T. Zhang, B. Zhou, Y. Zhang, Y. Guo, M. Rahn *et al.*, *Nat. Phys.* **11**, 728 (2015).  
 [18] B. Lv, H. Weng, B. Fu, X. Wang, H. Miao, J. Ma, P. Richard, X. Huang, L. Zhao, G. Chen *et al.*, *Phys. Rev. X* **5**, 031013 (2015).  
 [19] H. Chen, Q. Niu, and A. H. MacDonald, *Phys. Rev. Lett.* **112**, 017205 (2014).  
 [20] S. Nakatsuji, N. Kiyohara, and T. Higo, *Nature (London)* **527**, 212 (2015).  
 [21] A. K. Nayak, J. E. Fischer, Y. Sun, B. Yan, J. Karel, A. C. Komarek, C. Shekhar, N. Kumar, W. Schnelle, J. Kübler *et al.*, *Sci. Adv.* **2**, e1501870 (2016).  
 [22] N. Kiyohara, T. Tomita, and S. Nakatsuji, *Phys. Rev. Applied* **5**, 064009 (2016).  
 [23] H. Yang, Y. Sun, Y. Zhang, W.-J. Shi, S. S. Parkin, and B. Yan, *New J. Phys.* **19**, 015008 (2017).  
 [24] J. Kübler and C. Felser, *Europhys. Lett.* **108**, 67001 (2014).  
 [25] S. Tomiyoshi and Y. Yamaguchi, *J. Phys. Soc. Jpn.* **51**, 2478 (1982).  
 [26] P. Brown, V. Nunez, F. Tasset, J. Forsyth, and P. Radhakrishna, *J. Phys. Condens. Matter* **2**, 9409 (1990).  
 [27] E. Kren, J. Paitz, G. Zimmer, and E. Zsoldos, *Physica (Amsterdam)* **80**, 226 (1975).  
 [28] T. Nagamiya, S. Tomiyoshi, and Y. Yamaguchi, *Solid State Commun.* **42**, 385 (1982).  
 [29] See Supplemental Material at <http://link.aps.org/supplemental/10.1103/PhysRevLett.119.087202> for the details on the microscopic and continuum spin models, the electronic tight-binding model, the bulk and domain-wall transport properties, as well as the symmetry analysis on spin-transfer torques.  
 [30] M. Kardar, *Statistical Physics of Fields* (Cambridge University Press, Cambridge, 2007).  
 [31] C.-X. Liu, P. Ye, and X.-L. Qi, *Phys. Rev. B* **87**, 235306 (2013).  
 [32] D. C. Ralph and M. D. Stiles, *J. Magn. Magn. Mater.* **320**, 1190 (2008).  
 [33] S. Nakatsuji and Y. Otani [private communication].